

Shape of my heart: Cardiac models through learned signed distance functions

Jan Verhülsdonk^{*1}

VERHUELSDONK@IAM.UNI-BONN.DE

Thomas Grandits^{*2,4}

THOMAS.GRANDITS@UNI-GRAZ.AT

Francisco Sahli Costabal³

FSC@ING.PUC.CL

Thomas Pinetz¹

PINETZ@IAM.UNI-BONN.DE

Rolf Krause^{4,5}

ROLF.KRAUSE@USI.CH

Angelo Auricchio^{4,6}

ANGELO.AURICCHIO@EOC.CH

Gundolf Haase²

GUNDOLF.HAASE@UNI-GRAZ.AT

Simone Pezzuto^{4,7}

SIMONE.PEZZUTO@UNITN.IT

Alexander Effland¹

EFFFLAND@IAM.UNI-BONN.DE

¹ *Institute for Applied Mathematics, University of Bonn, Germany*

² *Department of Mathematics and Scientific Computing, University of Graz, Austria*

³ *Institute for Biological and Medical Engineering, Pontificia Universidad Católica de Chile, Chile*

⁴ *Center for Computational Medicine in Cardiology, Università della Svizzera italiana, Switzerland*

⁵ *FernUni Schweiz, Brig, Switzerland*

⁶ *Instituto Cardiocentro Ticino, EOC, Switzerland*

⁷ *Department of Mathematics, University of Trento, Italy*

Abstract

The efficient construction of anatomical models is one of the major challenges of patient-specific in-silico models of the human heart. Current methods frequently rely on linear statistical models, allowing no advanced topological changes, or requiring medical image segmentation followed by a meshing pipeline, which strongly depends on image resolution, quality, and modality. These approaches are therefore limited in their transferability to other imaging domains. In this work, the cardiac shape is reconstructed by means of three-dimensional deep signed distance functions with Lipschitz regularity. For this purpose, the shapes of cardiac MRI reconstructions are learned to model the spatial relation of multiple chambers. We demonstrate that this approach is also capable of reconstructing anatomical models from partial data, such as point clouds from a single ventricle, or modalities different from the trained MRI, such as the electroanatomical mapping (EAM).

Keywords: Deep Signed Distance Function, Shape Reconstruction, Cardiac Modeling, Lipschitz Regularized Network

1. Introduction

Modern personalized precision medicine frequently targets patient-specific therapies with improved therapy outcomes, reduced intervention times, and thus lower costs. In the case of cardiac personalized treatment, this necessitates complex simulation models from patient data [Corral-Acero et al. \(2020\)](#). This future vision of personalized cardiac treatment relies on generated 3D models, which should represent the anatomy of the corresponding patient.

* Contributed equally

Current methods to generate anatomical models usually require computed tomography (CT) or magnetic resonance (MR) images, which are segmented and subsequently meshed (Strocchi et al., 2020a). Yet, while automatic cardiac image segmentation is well-researched and constantly improving thanks to machine learning (Painchaud et al., 2020; Campello et al., 2021; Zhuang et al., 2022), it is limited to a specific image modality and resolution. Other modalities such as electroanatomical catheter mapping (Bhakta and Miller, 2008) are difficult to fit within standard frameworks, albeit they are very important for patient-specific modelling (Ruiz-Herrera et al., 2022).

In this work, we propose the use of implicitly learned representations through signed distance functions (SDFs). We start from the *DeepSDF* method (Park et al., 2019), which encodes SDF-based surfaces through a decoder-only neural network with a small-dimensional input latent code. The resulting neural network is a cardiac shape atlas. Shape inference can be achieved from location measurements such as electro-anatomical mappings and is applicable to arbitrary resolutions. Additionally, interpolation in the latent space yields shape interpolation in the physical space, a useful feat to create novel shapes. Differently from the original *DeepSDF* method, here we take advantage of Lipschitz-regularized neural networks (Liu et al., 2022) so to avoid overfitting of the network and to enforce smooth interpolations between samples in the latent space. This method is especially efficient for learning on relatively small training sets as considered here.

We demonstrate that this Lipschitz-regularized *DeepSDF* architecture is suited for constructing cardiac models by learning from a database of 44 publicly available, post-processed cardiac models. The resulting *DeepSDF* model is designed to encode bi-ventricular shapes and also infer new shapes from sparse point clouds, even if only partial domains are available (e.g., only endocardial measurements of a single chamber often encountered in electroanatomical mappings). The proposed method shares some similarities with the very recent work by Sander et al. (2023); however, our approach exhibits several major advantages compared with this paper: 1. applying a *Lipschitz-regularized* version of *DeepSDF* methodology to the cardiac domain on the example of bi-ventricular models and demonstrating advantageous accuracy in the presence of sparse data in comparison to state-of-the-art methods, 2. thanks to the multi-chamber approach both topological constraints are implicitly incorporated and adjacent anatomical structures benefit from additional available data, which might also aid uncertainty quantification in future research, 3. our approach is more robust against measurement errors modeling noise due to the iterative noise estimation and the additional prior penalization, which allows for the reconstruction of cardiac shapes from in-vivo measurements of an electroanatomical mapping procedure.

2. Related work

Surface reconstruction from point clouds is an intensively researched topic and provides a variety of possible approaches (Ma et al., 2022). Classical approaches assume no prior knowledge of the given point clouds, but in turn, require dense point clouds and are often sensitive to noise (Carr et al., 2001; Kazhdan et al., 2006; Kazhdan and Hoppe, 2013; Umhoefer and Brox, 2015; Fuhrmann and Goesele, 2014). Modern deep-learning approaches try to overcome these limitations by learning prior information about shapes using learned

SDFs (Park et al., 2019; Hanocka et al., 2020), occupancy fields (Mescheder et al., 2019), level sets (Michalkiewicz et al., 2019) or implicit fields (Chen and Zhang, 2019).

In this context, the *DeepSDF* method is one of the most active fields of research. Such methods usually try to infer a multitude of shapes from at least partially dense point clouds. However, this method is prone to overfitting the data, thus often requiring regularization both in the latent space, as well as in the neural network by imposing dropout rules (Park et al., 2019). In Liu et al. (2022), Lipschitz-regularized linear layers are proposed, which are able to overcome some of these limitations. Alternative forms of regularization are, for instance, based on the eikonal equation (Gropp et al., 2020), other methods rely on local SDFs (Chabra et al., 2020; Jiang et al., 2020; Tretschk et al., 2020; Erler et al., 2020), neural-pulls (Baorui et al., 2021), or learned unsigned distance functions (Chibane et al., 2020). For further methods and comparisons, we refer the reader to Ma et al. (2022).

Statistical Shape Models (SSMs) are classical methods for (cardiac) shape reconstruction, which are tailored to the whole heart (Ecabert et al., 2008; Hoogendoorn et al., 2013; Lötjönen et al., 2004; Ordas et al., 2007; Unberath et al., 2015; Zhuang et al., 2010), the atria (Nagel et al., 2021), or the ventricles (Bai et al., 2015; Petersen et al., 2017). Only a few works have shown that deep learning methods can be applied to the cardiac domain to reconstruct cardiac shapes from point clouds (Beetz et al., 2023; Kong et al., 2023; Xiong et al., 2022; Sander et al., 2023; Alblas et al., 2023; Wang et al., 2021), whereas most of the learning based methods heavily rely on image input (Beetz et al., 2022; Kong et al., 2021).

3. Method

In this section, we comment on the representation of cardiac shapes by learned SDFs and provide details about training and shape completion.

3.1. General setting

We assume that each shape describing the heart is volumetrically represented as an SDF given by $f_S : \mathbb{R}^3 \rightarrow \mathbb{R}$ mapping from spatial points $\mathbf{x} \in \mathbb{R}^3$ to their respective signed distances $s \in \mathbb{R}$. These signed distances encode the signed projection distance at a point \mathbf{x} to the surface (negative values inside, positive values outside). In such a way, the cardiac surface is represented as the zero-level set of this SDF, i.e., $\{\mathbf{x} \in \mathbb{R}^3 : f_S(\mathbf{x}) = 0\}$. A straightforward approach to learning such an SDF for arbitrary shapes involves representing the SDF by a neural network $S_\theta : \mathbb{R}^3 \rightarrow \mathbb{R}$, in which case the SDF is fully defined by the network’s architecture and weights θ . However, modeling surfaces solely through their neural network weights would necessitate a separate SDF and subsequent neural network for each individual surface, while also neglecting any similarities between the available training shapes. Following (Park et al., 2019), we instead model all shapes using a single neural network and additionally provide this network with a d -dimensional latent representation $\mathbf{z} \in \mathbb{R}^d$ of the shape as an additional input, together with the aforementioned spatial coordinates, i.e. $S_\theta : \mathbb{R}^{3+d} \rightarrow \mathbb{R}$. Hence, we encode multiple heart geometries with the same network, but different latent codes. We propose to model each of the left and right endocardial and epicardial surfaces with a shared latent code and neural network by letting the DeepSDF simultaneously estimate a signed distance for each of the closed bi-ventricular surfaces $\mathbf{s} =$

$(s_1, s_2, s_3, s_4)^\top \in \mathbb{R}^4$. In summary, the learned DeepSDF is given by the vector-valued function $\mathbf{S}_\theta : \mathbb{R}^{3+d} \rightarrow \mathbb{R}^4$.

3.2. Training and network architecture

The anatomical samples $X_i := (\mathbf{x}_k, \mathbf{s}_k)_{k=1}^{K_i}$ used for learning are K_i pairs of spatial coordinates \mathbf{x}_k with their sampled signed distance vector \mathbf{s}_k for the i -th biventricular shape. The set of all N available anatomical bi-ventricular samples is denoted as $X := (X_i)_{i=1}^N$. To each anatomical shape i , we associate a coupled latent code representation $\mathbf{z}_i \in \mathbb{R}^d$ also learned from data. We denote the set of learned latent codes as $Z := (\mathbf{z}_i)_{i=1}^N$. Our goal during training is to minimize the mismatch between the sampled signed distances and the ones estimated by the network through a simple quadratic loss term. Additionally, to restrict the latent codes Z , we follow (Park et al., 2019) and assume a zero mean Gaussian prior distribution with covariance $\sigma^2 I$ on the latent codes, which gives rise to the loss term

$$\mathcal{L}(\theta, Z) = \frac{1}{N} \sum_{i=1}^N \sum_{(\mathbf{x}_k, \mathbf{s}_k) \in X_i} \frac{1}{4K_i} \|\mathbf{S}_\theta(\mathbf{x}_k, \mathbf{z}_i) - \mathbf{s}_k\|^2 + \frac{1}{\sigma^2} \|\mathbf{z}_i\|_2^2.$$

The parameter σ is used to balance between reconstruction accuracy for the training shapes and regularity in the latent space, which is essential for shape completion as described in Section 3.3. See Section 4.1 for the choice of σ in our model. In Liu et al. (2022), it was shown that learning \mathcal{L} directly may result in overfitting and might provide poor interpolation properties for the latent space. To overcome these issues, a Lipschitz penalization on the network was proposed in order to better control the smoothness. For this purpose, the Lipschitz bound L of the network is estimated by $L = \prod_{i=1}^M \|W_i\|_p$ for an M -layer deep network, where W_i are the network weights of the i -th layer. We closely follow the implementation of (Liu et al., 2022) where the linear layers of our network are replaced with Lipschitz-normalized layers. For each layer an additional weight c_i is introduced such that $\text{softplus}(c_i) = \ln(1 + e^{c_i})$ serves as an upper bound $\text{softplus}(c_i) \geq \|W_i\|_p$ for the Lipschitz constant. Integrating this Lipschitz-regularization into our previous loss-functional \mathcal{L} leads to our finally used cost-functional

$$J(\theta, Z) = \mathcal{L}(\theta, Z) + \alpha \prod_{c_i \in C(\theta)} \text{softplus}(c_i), \quad (1)$$

where $C(\theta) = (c_i)_{i=1}^M$ denotes the network parameter dependent per-layer Lipschitz bounds.

As mentioned, for samples $X_i := (\mathbf{x}_k, \mathbf{s}_k)_{k=1}^{K_i}$ the network inputs are the latent code \mathbf{z}_i and the spatial coordinates \mathbf{x}_i of the sample point. Following Liu et al. (2022) the spatial coordinates are multiplied by the factor $C_s = 100$ to balance the Lipschitz regularity of the latent space and the spatial coordinates. We use 5 hidden layers with 256 neurons and tanh activation functions. In the third hidden layer, the latent code and the spatial coordinate are concatenated to the output of the previous layer. The last layer is a linear layer with four signed distance functions as output, one for each of the left, right, epi- and endocardial surfaces. The latent code size was chosen as $d = 64$. A schematic representation of the network is shown in Figure 1 (left).

For the training of our network, we built a public shape library of watertight 3D shapes for endo-/epicardium of the left/right ventricles (Grandits et al., 2024) (4 shapes in total)

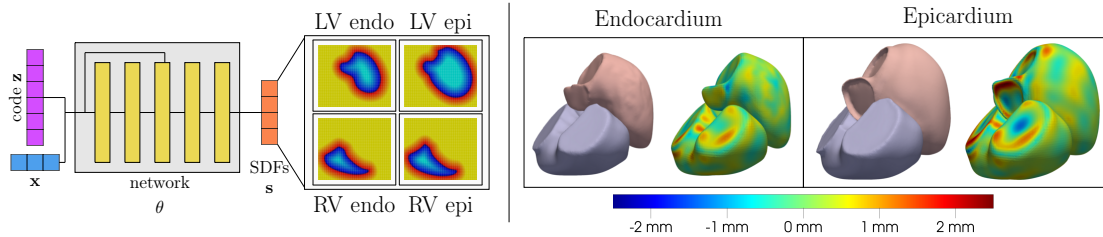


Figure 1: Left: a schematic representation of the employed DeepSDF. Right: comparison of ground truth meshes (LV in red, RV in blue) with reconstruction on the training dataset. The reconstructed meshes are color-coded with the signed distance to the ground truth mesh in mm.

based on [Rodero et al. \(2021\)](#); [Strocchi et al. \(2020b\)](#). Further details on the construction of the training data is provided in [appendix A](#).

3.3. Shape completion

After learning the SDF network, a new anatomical bi-ventricular shape can be inferred from sparse point clouds of any combination of surfaces or given signed distance. For this, we consider K given samples consisting of triplets \tilde{Y} of spatial coordinates $\mathbf{x}_k \in \mathbb{R}^3$, a single signed distance $s_k \in \mathbb{R}$, and an index of the surface $j_k \in \{1, 2, 3, 4\}$. If a point \mathbf{x}_k lies on the surface j_k , then $s_k = 0$. Finding the bi-ventricular reconstruction of a point cloud thus reduces to finding its latent code representation \mathbf{z} by minimizing the following problem

$$\min_{\mathbf{z}} \frac{1}{K} \sum_{(\mathbf{x}_k, s_k, j_k) \in \tilde{Y}} \left((\mathbf{S}_\theta(\mathbf{x}_k, \mathbf{z}))_{j_k} - s_k \right)^2 + \frac{\beta}{\sigma^2} \|\mathbf{z}\|_2^2, \quad (2)$$

where the subscript refers to the vector component and β is an additional weight that is increased depending on the noise of the input point cloud. For noise-free point clouds, we set $\beta = 1$ to obtain the maximum-a-posterior (MAP) estimation ([Park et al., 2019](#)).

For noisy input point clouds, the expected data loss of a perfect reconstruction can be approximated with the variance of the noise ξ . We set $\beta = C_b \xi$, where $C_b = 100$ is a chosen scaling factor. In the case of real-world data, the underlying noise structure is unknown and estimated as follows: We start with a reconstruction \mathbf{S}_θ^0 for an arbitrary initial noise estimation ξ_0 . We then iteratively estimate the *empirical variance* $\bar{\xi}_{n+1}^2$ based on \mathbf{S}_θ^n via

$$\bar{\xi}_{n+1}^2 = \frac{1}{K-1} \sum_{(\mathbf{x}_k, s_k, j_k) \in \tilde{Y}} \left((\mathbf{S}_\theta^n(\mathbf{x}_k, \mathbf{z}))_{j_k} - s_k \right)^2. \quad (3)$$

This estimation exhibits a high experimental convergence rate (see [appendix Section F](#)).

4. Experiments

In this section, we state details of the training procedure and the network architecture. Moreover, we introduce distinct metrics for the evaluation of the surface reconstruction quality, which are exploited in all benchmarks. Finally, we evaluate the network on in-vivo measured catheter data.

4.1. Numerical experiments

In this section, we present the numerical results obtained with the proposed method. During the training process, we optimize both the network parameters θ and the latent code representations \mathbf{z}_i of the training data. The network is fit to 4 surfaces, namely the epi- and endocardium of the right and left ventricle, and the associated hyperparameters σ and α are optimized for the best performance of the reconstruction in the shape completion process. For the loss term, we thus obtained $1/\sigma^2 \approx 1.8 \times 10^{-7}$ and $\alpha = 1.9 \times 10^{-6}$. The network is trained with the Adam optimizer (Kingma and Ba, 2015) for 3000 epochs with a learning rate of 0.005 which is decreased twice with the factor of 0.2 after 2700 and 2900 epochs. For the mesh generation, we compute the signed distance function on a 128^3 grid on the bounding box of all training points and reconstruct the zero-level set using the contour filter of PyVista (Sullivan and Kaszynski, 2019), based on marching cubes. The final reconstruction quality of the training models is depicted in Figure 1 (right).

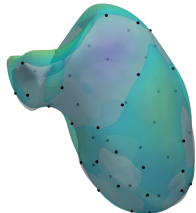
We test the regularity of our network with respect to the latent space input with inter- and extrapolation between two latent codes of the training dataset. The shapes of the reconstructed hearts change uniformly between every inter- and extrapolation point and generate meaningful results (see appendix Figure 4). Points that are drawn from the prior distribution with covariance $\sigma^2 I$ produce meaningful heart geometries (see appendix Figure 5). With our model, we are able to learn multiple implicit surfaces at the same time and encode them in a joint latent space representation. Therefore, it is easily possible to calculate the latent code during inference time based on an arbitrary subset of surface points. We test this by sampling sparse point clouds on the endocardium of the left ventricles from the test set and optimizing the latent code according to (2), still providing us with a full 4-chamber biventricular shape. Not only is our method capable of a close reconstruction of the endocardium of the left ventricle, but it can also predict possible shapes of the other three surfaces. We provide visual results for a reconstruction from 50 lv endocardial points in Figure 2 and Figure 6. Note however that the accuracy of the unmeasured right ventricular shape significantly decreases. Numerical results of the reconstruction quality on the endocardium of the left ventricle can be found in Section 4.2.

4.2. Validation

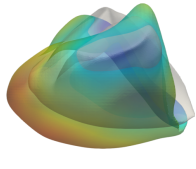
Our method is compared with Points2Surf (Erler et al., 2020), Point2Mesh (Hanocka et al., 2020), and a variant of our network without Lipschitz regularization. In all experiments, only the endocardium of the left ventricle is considered. All methods are compared on point clouds with different cardinalities n , ranging from very sparse point clouds with $n = 50$ to relatively dense ones with $n = 2000$. Additionally, the coordinates of the points are perturbed with noise drawn from a Gaussian normal distribution with zero mean and fixed covariance $\xi^2 I$. For each number of points n and level of noise ξ we test the methods on the same 44-point clouds sampled from the meshes of the data set (for Points2Surf we apply a pre-trained model (Erler et al., 2020)). In the appendix we additionally provide a comparison to a SSM (see Appendix C). To test our method on all 44 meshes of the dataset we selected 11 disjoint test sets and train a different network on each remaining training sets. For both our unregularized ($\alpha = 0$) and regularized DeepSDF we take $\beta = \max(1, C_s \xi^2)$ and minimize the objective in (2) using the Adam optimizer (Kingma and Ba, 2015) with

	ξ	n	Points2Surf	Point2Mesh	ours*	ours
Chamfer Distance	0	50	-	1.74 ± 0.41	1.2 ± 0.91	0.75 ± 0.18
		200	-	<i>0.68 ± 0.11</i>	0.72 ± 0.54	0.49 ± 0.09
		500	1.66 ± 0.32	<i>0.57 ± 0.08</i>	0.70 ± 0.57	0.45 ± 0.09
	2	50	-	2.33 ± 0.54	<i>1.65 ± 0.87</i>	1.38 ± 0.28
		200	-	<i>1.16 ± 0.13</i>	1.16 ± 0.57	0.96 ± 0.17
		500	1.65 ± 0.14	<i>0.97 ± 0.10</i>	<i>0.97 ± 0.33</i>	0.96 ± 0.11
	5	50	-	3.50 ± 0.49	<i>2.6 ± 0.98</i>	2.39 ± 0.48
		200	-	3.17 ± 0.62	<i>1.87 ± 0.39</i>	1.84 ± 0.27
		500	2.82 ± 0.31	3.85 ± 1.15	<i>2.32 ± 1.00</i>	1.99 ± 0.33

LV Endo



RV Endo



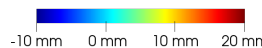


Figure 2: Left: mean and standard deviation of the Chamfer distance (CD) for different numbers of input points n and different levels of noise ξ (lowest value in **bold magenta**, second lowest value in *teal and italic*; short version of Table 1 in the appendix). The asterisk denotes the non Lipschitz regularized version of our network. Right: reconstruction of both endocardia from points on the LV endocardium (gt mesh in grey, reconstruction color-coded with implicit distance).

a learning rate of 10^{-2} for 50 000 epochs. In our unregularized network we used standard linear layers without any regularization and changed the activation functions to ReLU. For the unregularized layers this seems to improve the performance drastically, whereas for the regularized case we found that the choice of activation function did not influence the results too much. The results for $n = 50$ on four meshes computed with our method are depicted in Figure 7 in the appendix. For the comparison, we evaluated the performance in terms of *L2-Chamfer-distance* (CD), which can be seen in Figure 2. For two point clouds \mathbf{X} and \mathbf{Y} the CD is given as $d_{\text{CD}}(\mathbf{X}, \mathbf{Y}) = \frac{1}{|\mathbf{X}|} \sum_{x \in \mathbf{X}} \min_{y \in \mathbf{Y}} \|x - y\|_2 + \frac{1}{|\mathbf{Y}|} \sum_{y \in \mathbf{Y}} \min_{x \in \mathbf{X}} \|x - y\|_2$. In appendix B and Table 1 further comparisons in terms of *Hausdorff-distance* (HD), and *Large deformation diffeomorphic metric mapping* (LDDMM) with their respective definitions are provided. For every test case, we state the mean and standard deviation across the four meshes of the test set. Note that Points2Surf did not converge for sparse point clouds ($n = 50$ and $n = 200$). We thus omitted the associated results in the table. Our method performs particularly well on sparse point clouds compared to the other methods. The obtained meshes are qualitatively similar to the ground truth meshes and geometric features like the curvature can be recovered properly (see appendix Figure 8).

4.3. Inference from electroanatomical mapping data

Electro-anatomical mapping (EAM) is a common routine for patients undergoing catheter ablation. As the catheter is inserted into the heart, it continuously builds a three-dimensional point cloud that is triangulated into a surface model. Our EAM data consists of a set of points located on the endocardial surface of the left ventricle. The point cloud is usually sparse and unevenly distributed, but commonly allows for a reasonable estimate of endocardial geometry. The exact data acquisition process is described in detail in appendix E. The

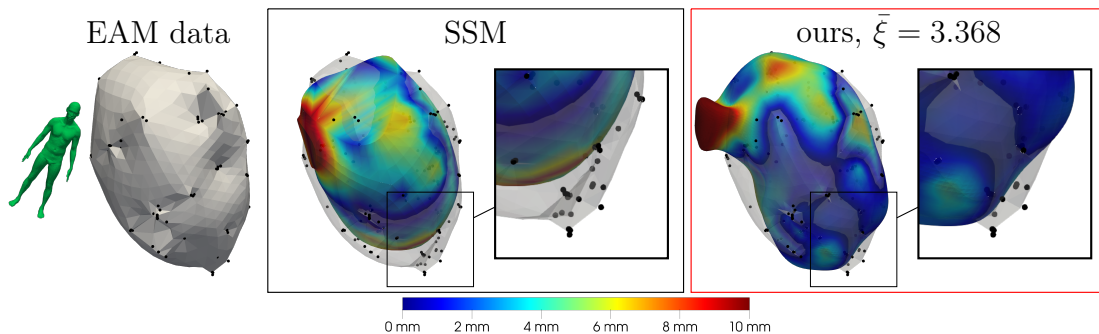


Figure 3: Reconstruction of the LV endocardium from the EAM data. We compare the SSM reconstruction (left panel) to our approach for an optimal noise level estimation of $\bar{\sigma} = 3.368$ mm (right panel). We also report the absolute distance from the geometry provided by the EAM system.

overall LV shape is well-approximated in most regions except for the apex, as can be seen in Figure 3 and Figure 9, and includes the outflow aortic tract due to the learned modality. Compared to the LV surface obtained from the EAM system, our shape is much smoother and is even defined in regions where data is missing. Since the underlying noise structure is unknown, we estimate the noise variance iteratively as described in (3). For the EAM data, we obtain an estimate of 3.4 mm, consistent with the size of the electrode’s tip (2 – 4 mm). A table containing the iterates of the estimator can be found in Table 3 in the appendix.

5. Discussion and outlook

We have presented a novel method to represent cardiac anatomy based on signed-distance functions. The quantitative comparison with other methods shows that our approach can reconstruct the shape of hearts on a state-of-the-art level, especially for sparse and noisy data. In contrast to the methods we compared against, our approach does not require knowledge of the normals at each point of the point cloud. This knowledge however could be incorporated at the shape completion stage by fitting the normalized gradient of the SDF against the given normals.

The requirement of point clouds is a mixed blessing, as it requires the construction of a point cloud from images through a learned method, or by segmenting the image stack and using its surface. On the other hand, enables the algorithm to operate on different modalities. Additionally, the algorithm expects the point clouds in a canonical pose (CT-based), which however could be automated using rigid point registration methods [Jian and Vemuri \(2010\)](#). Learning multiple SDFs with one network allows the generation of shapes based on input data from different chambers of the heart or a combination of multiple surfaces.

While the present work only encodes bi-ventricular surfaces, the method itself can be extended to encode additional chambers and shapes, such as the atria or aorta. This method has important implications in cardiac modeling, digital twinning for precision medicine, and the creation of virtual cohort of patients. We plan to further extend it to time-dependent shape models and shape uncertainty quantification ([Gander et al., 2021](#)).

6. Acknowledgements

This work was supported by the Swiss National Science Fund [Cardiotwin, Weave/Lead Agency, Project number 214817], by the Deutsche Forschungsgemeinschaft (DFG, German Research Foundation) [EXC-2047/1-390685813] and [EXC2151-390873048], PRIN-PNRR [project no. P2022N5ZNP], and Swiss National Supercomputing Centre [production grant no. s1074].

References

- Dieuwertje Alblas, Christoph Brune, Kak Khee Yeung, and Jelmer M Wolterink. Going off-grid: Continuous implicit neural representations for 3d vascular modeling. In *Statistical Atlases and Computational Models of the Heart. Regular and CMRxMotion Challenge Papers: 13th International Workshop, STACOM 2022, Held in Conjunction with MICCAI 2022, Singapore, September 18, 2022, Revised Selected Papers*, pages 79–90. Springer, 2023.
- W Bai, W Shi, A de Marvao, TJ Dawes, DP O’Regan, SA Cook, and D Rueckert. A bi-ventricular cardiac atlas built from 1000+ high resolution mr images of healthy subjects and an analysis of shape and motion. *Med Image Anal.*, 26(1):133–45, 2015.
- Ma Baorui, Han Zhizhong, Liu Yu-Shen, and Zwicker Matthias. Neural-pull: Learning signed distance functions from point clouds by learning to pull space onto surfaces. In *International Conference on Machine Learning (ICML)*, 2021.
- Jason Bayer, Anton J. Prassl, Ali Pashaei, Juan F. Gomez, Antonio Frontera, Aurel Neic, Gernot Plank, and Edward J. Vigmond. Universal ventricular coordinates: A generic framework for describing position within the heart and transferring data. *Medical Image Analysis*, 45:83–93, April 2018. ISSN 1361-8415.
- Marcel Beetz, Jorge Corral Acero, Abhirup Banerjee, Ingo Eitel, Ernesto Zacur, Torben Lange, Thomas Stiermaier, Ruben Evertz, Sören J. Backhaus, Holger Thiele, Alfonso Bueno-Orovio, Pablo Lamata, Andreas Schuster, and Vicente Grau. Interpretable cardiac anatomy modeling using variational mesh autoencoders. *Frontiers in Cardiovascular Medicine*, 9, 2022. ISSN 2297-055X.
- Marcel Beetz, Abhirup Banerjee, and Vicente Grau. Point2mesh-net: Combining point cloud and mesh-based deep learning for cardiac shape reconstruction. In *Statistical Atlases and Computational Models of the Heart. Regular and CMRxMotion Challenge Papers: 13th International Workshop, STACOM 2022, Held in Conjunction with MICCAI 2022, Singapore, September 18, 2022, Revised Selected Papers*, pages 280–290. Springer, 2023.
- Deepak Bhakta and John M Miller. Principles of electroanatomic mapping. *Indian pacing and electrophysiology journal*, 8(1):32, 2008. Publisher: Elsevier.
- Blender Online Community. *Blender - a 3D modelling and rendering package*. Blender Foundation, Stichting Blender Foundation, Amsterdam, 2018.

- Víctor M. Campello, Polyxeni Gkontra, Cristian Izquierdo, Carlos Martín-Isla, Alireza Sojoudi, Peter M. Full, Klaus Maier-Hein, Yao Zhang, Zhiqiang He, Jun Ma, Mario Parreño, Alberto Albiol, Fanwei Kong, Shawn C. Shadden, Jorge Corral Acero, Vaanathi Sundaresan, Mina Saber, Mustafa Elattar, Hongwei Li, Bjoern Menze, Firas Khader, Christoph Haarbuerger, Cian M. Scannell, Mitko Veta, Adam Carscadden, Kumaradevan Punithakumar, Xiao Liu, Sotirios A. Tsaftaris, Xiaoqiong Huang, Xin Yang, Lei Li, Xiahai Zhuang, David Viladés, Martín L. Descalzo, Andrea Guala, Lucia La Mura, Matthias G. Friedrich, Ria Garg, Julie Lebel, Filipe Henriques, Mahir Karakas, Ersin Çavuş, Steffen E. Petersen, Sergio Escalera, Santi Seguí, José F. Rodríguez-Palomares, and Karim Lekadir. Multi-Centre, Multi-Vendor and Multi-Disease Cardiac Segmentation: The M&Ms Challenge. *IEEE Transactions on Medical Imaging*, 40(12):3543–3554, December 2021. ISSN 1558-254X. Conference Name: IEEE Transactions on Medical Imaging.
- Jonathan C Carr, Richard K Beatson, Jon B Cherrie, Tim J Mitchell, W Richard Fright, Bruce C McCallum, and Tim R Evans. Reconstruction and representation of 3d objects with radial basis functions. In *Proceedings of the 28th annual conference on Computer graphics and interactive techniques*, pages 67–76, 2001.
- Rohan Chabra, Jan E Lenssen, Eddy Ilg, Tanner Schmidt, Julian Straub, Steven Lovegrove, and Richard Newcombe. Deep local shapes: Learning local sdf priors for detailed 3d reconstruction. In *Computer Vision—ECCV 2020: 16th European Conference, Glasgow, UK, August 23–28, 2020, Proceedings, Part XXIX 16*, pages 608–625. Springer, 2020.
- Zhiqin Chen and Hao Zhang. Learning implicit fields for generative shape modeling. In *Proceedings of the IEEE/CVF Conference on Computer Vision and Pattern Recognition*, pages 5939–5948, 2019.
- Julian Chibane, Gerard Pons-Moll, et al. Neural unsigned distance fields for implicit function learning. *Advances in Neural Information Processing Systems*, 33:21638–21652, 2020.
- Jorge Corral-Acero, Francesca Margara, Maciej Marciniak, Cristobal Rodero, Filip Loncaric, Yingjing Feng, Andrew Gilbert, Joao F Fernandes, Hassaan A Bukhari, Ali Wajdan, Manuel Villegas Martinez, Mariana Sousa Santos, Mehrdad Shamohammdi, Hongxing Luo, Philip Westphal, Paul Leeson, Paolo DiAchille, Viatcheslav Gurev, Manuel Mayr, Liesbet Geris, Pras Pathmanathan, Tina Morrison, Richard Cornelussen, Frits Prinzen, Tammo Delhaas, Ada Doltra, Marta Sitges, Edward J Vigmond, Ernesto Zacur, Vicente Grau, Blanca Rodriguez, Espen W Remme, Steven Niederer, Peter Mortier, Kristin McLeod, Mark Potse, Esther Pueyo, Alfonso Bueno-Orovio, and Pablo Lamata. The ‘Digital Twin’ to enable the vision of precision cardiology. *European Heart Journal*, 41(48):4556–4564, December 2020. ISSN 0195-668X.
- Michael Dawson-Haggerty et al. trimesh, 2009. URL <https://trimsh.org/>.
- Olivier Ecabert, Jochen Peters, Hauke Schramm, Cristian Lorenz, Jens von Berg, Matthew J. Walker, Mani Vembar, Mark E. Olszewski, Krishna Subramanyan, Guy Lavi, and Jürgen Weese. Automatic model-based segmentation of the heart in ct images. *IEEE Transactions on Medical Imaging*, 27(9):1189–1201, 2008.

- Philipp Erler, Paul Guerrero, Stefan Ohrhallinger, Niloy J. Mitra, and Michael Wimmer. Points2surf learning implicit surfaces from point clouds. In *Computer Vision – ECCV 2020*, pages 108–124. Springer International Publishing, 2020.
- Simon Fuhrmann and Michael Goesele. Floating scale surface reconstruction. *ACM Transactions on Graphics (ToG)*, 33(4):1–11, 2014.
- Lia Gander, Rolf Krause, Michael Multerer, and Simone Pezzuto. Space-time shape uncertainty in the forward and inverse problem of electrocardiography. *International Journal for Numerical Methods in Biomedical Engineering*, 37, 2021.
- Tingran Gao, Shahar Z. Kovalsky, and Ingrid Daubechies. Gaussian Process Landmarking on Manifolds. *SIAM Journal on Mathematics of Data Science*, 1(1):208–236, January 2019. Publisher: Society for Industrial and Applied Mathematics.
- Thomas Grandits. A Fast Iterative Method Python package. *Journal of Open Source Software*, 6(66):3641, October 2021. ISSN 2475-9066.
- Thomas Grandits, Jan Verhülsdonk, Francisco Sahli Costabal, Thomas Pinetz, Alexander Effland, and Simone Pezzuto. A public manifold left/right ventricular database, May 2024. URL <https://zenodo.org/records/7687883>.
- Amos Gropp, Lior Yariv, Niv Haim, Matan Atzmon, and Yaron Lipman. Implicit geometric regularization for learning shapes, 2020.
- Rana Hanocka, Gal Metzer, Raja Giryes, and Daniel Cohen-Or. Point2mesh: A self-prior for deformable meshes. *ACM Trans. Graph.*, 39(4), 2020. ISSN 0730-0301.
- Corné Hoogendoorn, Nicolas Duchateau, Damián Sanchez-Quintana, Tristan Whitmarsh, Federico M. Sukno, Mathieu De Craene, Karim Lekadir, and Alejandro F. Frangi. A high-resolution atlas and statistical model of the human heart from multislice ct. *IEEE Transactions on Medical Imaging*, 32(1):28–44, 2013.
- Bing Jian and Baba C Vemuri. Robust point set registration using gaussian mixture models. *IEEE transactions on pattern analysis and machine intelligence*, 33(8):1633–1645, 2010.
- Chiyu Jiang, Avneesh Sud, Ameesh Makadia, Jingwei Huang, Matthias Nießner, Thomas Funkhouser, et al. Local implicit grid representations for 3d scenes. In *Proceedings of the IEEE/CVF Conference on Computer Vision and Pattern Recognition*, pages 6001–6010, 2020.
- Michael Kazhdan and Hugues Hoppe. Screened poisson surface reconstruction. *ACM Transactions on Graphics (ToG)*, 32(3):1–13, 2013.
- Michael Kazhdan, Matthew Bolitho, and Hugues Hoppe. Poisson surface reconstruction. In *Proceedings of the fourth Eurographics symposium on Geometry processing*, volume 7, 2006.
- Diederik P Kingma and Jimmy Ba. Adam: A method for stochastic optimization. *The International Conference on Learning Representations (ICLR)*, 2015.

- Fanwei Kong, Nathan Wilson, and Shawn Shadden. A deep-learning approach for direct whole-heart mesh reconstruction. *Medical Image Analysis*, 74:102222, 2021. ISSN 1361-8415.
- Fanwei Kong, Sascha Stocker, Perry S Choi, Michael Ma, Daniel B Ennis, and Alison Marsden. Sdf4chd: Generative modeling of cardiac anatomies with congenital heart defects. *ArXiv; United States*, 2023.
- Hsueh-Ti Derek Liu, Francis Williams, Alec Jacobson, Sanja Fidler, and Or Litany. Learning smooth neural functions via lipschitz regularization. In *ACM SIGGRAPH 2022 Conference Proceedings*. Association for Computing Machinery, 2022.
- J. Lötjönen, S. Kivistö, J. Koikkalainen, D. Smutek, and K. Lauerma. Statistical shape model of atria, ventricles and epicardium from short- and long-axis mr images. *Medical Image Analysis*, 8(3):371–386, 2004. ISSN 1361-8415. Medical Image Computing and Computer-Assisted Intervention - MICCAI 2003.
- Baorui Ma, Yu-Shen Liu, Matthias Zwicker, and Zhizhong Han. Surface reconstruction from point clouds by learning predictive context priors. In *Proceedings of the IEEE/CVF Conference on Computer Vision and Pattern Recognition*, pages 6326–6337, 2022.
- Francesco Maffessanti, Tomasz Jadczyk, Radosław Kurzelowski, François Regoli, Maria Luce Caputo, Giulio Conte, Krzysztof S Gołba, Jolanta Biernat, Jacek Wilczek, Magdalena Dąbrowska, Simone Pezzuto, Tiziano Moccetti, Rolf Krause, Wojciech Wojakowski, Frits W Prinzen, and Angelo Auricchio. The influence of scar on the spatio-temporal relationship between electrical and mechanical activation in heart failure patients. *EP Europace*, 22(5):777–786, 2020.
- Lars Mescheder, Michael Oechsle, Michael Niemeyer, Sebastian Nowozin, and Andreas Geiger. Occupancy Networks: Learning 3D Reconstruction in Function Space. In *2019 IEEE/CVF Conference on Computer Vision and Pattern Recognition (CVPR)*, pages 4455–4465, June 2019. ISSN: 2575-7075.
- Mateusz Michalkiewicz, Jhony K Pontes, Dominic Jack, Mahsa Baktashmotlagh, and Anders Eriksson. Deep level sets: Implicit surface representations for 3d shape inference. *arXiv preprint arXiv:1901.06802*, 2019.
- Claudia Nagel, Steffen Schuler, Olaf Dössel, and Axel Loewe. A bi-atrial statistical shape model for large-scale in silico studies of human atria: Model development and application to ecg simulations. *Medical Image Analysis*, 74:102210, 2021. ISSN 1361-8415.
- Sebastian Ordas, Estanislao Oubel, Rafael Sebastian, and Alejandro F. Frangi. Computational anatomy atlas of the heart. In *2007 5th International Symposium on Image and Signal Processing and Analysis*, pages 338–342, 2007.
- Nathan Painchaud, Youssef Skandarani, Thierry Judge, Olivier Bernard, Alain Lalande, and Pierre-Marc Jodoin. Cardiac Segmentation With Strong Anatomical Guarantees. *IEEE Transactions on Medical Imaging*, 39(11):3703–3713, November 2020. ISSN 1558-254X. Conference Name: IEEE Transactions on Medical Imaging.

- Jeong Joon Park, Peter Florence, Julian Straub, Richard Newcombe, and Steven Lovegrove. Deepsdf: Learning continuous signed distance functions for shape representation. In *2019 IEEE/CVF Conference on Computer Vision and Pattern Recognition (CVPR)*, pages 165–174, 2019. doi: 10.1109/CVPR.2019.00025.
- Steffen E. Petersen, Nay Aung, Mihir M. Sanghvi, Filip Zemrak, Kenneth Fung, Jose Miguel Paiva, Jane M. Francis, Mohammed Y. Khanji, Elena Lukaschuk, Aaron M. Lee, Valentina Carapella, Young Jin Kim, Paul Leeson, Stefan K. Piechnik, and Stefan Neubauer. Reference ranges for cardiac structure and function using cardiovascular magnetic resonance (CMR) in Caucasians from the UK Biobank population cohort. *Journal of Cardiovascular Magnetic Resonance*, 19(1):18, February 2017. ISSN 1532-429X.
- Simone Pezzuto, Frits W. Prinzen, Mark Potse, Francesco Maffessanti, François Regoli, Maria Luce Caputo, Giulio Conte, Rolf Krause, and Angelo Auricchio. Reconstruction of three-dimensional biventricular activation based on the 12-lead electrocardiogram via patient-specific modelling. *EP Europace*, 23(4):640–647, 2021.
- Cristobal Rodero, Marina Strocchi, Maciej Marciniak, Stefano Longobardi, John Whitaker, Mark D. O’Neill, Karli Gillette, Christoph Augustin, Gernot Plank, Edward J. Vigmond, Pablo Lamata, and Steven A. Niederer. Virtual cohort of adult healthy four-chamber heart meshes from CT images, March 2021. URL <https://zenodo.org/record/4590294>. Type: dataset.
- Carlos Ruiz-Herrera, Thomas Grandits, Gernot Plank, Paris Perdikaris, Francisco Sahli Costabal, and Simone Pezzuto. Physics-informed neural networks to learn cardiac fiber orientation from multiple electroanatomical maps. *Engineering with Computers*, 2022.
- Jörg Sander, Bob D. de Vos, Steffen Bruns, Nils Planken, Max A. Viergever, Tim Leiner, and Ivana Išgum. Reconstruction and completion of high-resolution 3d cardiac shapes using anisotropic cmri segmentations and continuous implicit neural representations. *Computers in Biology and Medicine*, 164:107266, 2023. ISSN 0010-4825.
- Will Schroeder, Ken Martin, and Bill Lorensen. *The Visualization Toolkit (4th ed.)*. Kitware, 2006. ISBN 978-1-930934-19-1.
- Marina Strocchi, Christoph M. Augustin, Matthias A. F. Gsell, Elias Karabelas, Aurel Neic, Karli Gillette, Orod Razeghi, Anton J. Prassl, Edward J. Vigmond, Jonathan M. Behar, Justin Gould, Baldeep Sidhu, Christopher A. Rinaldi, Martin J. Bishop, Gernot Plank, and Steven A. Niederer. A publicly available virtual cohort of four-chamber heart meshes for cardiac electro-mechanics simulations. *PLOS ONE*, 15(6):e0235145, June 2020a. ISSN 1932-6203. Publisher: Public Library of Science.
- Marina Strocchi, Christoph M. Augustin, Matthias A. F. Gsell, Elias Karabelas, Aurel Neic, Karli Gillette, Orod Razeghi, Anton J. Prassl, Edward J. Vigmond, Jonathan M. Behar, Justin S. Gould, Baldeep Sidhu, Christopher A. Rinaldi, Martin J. Bishop, Gernot Plank, and Steven A. Niederer. A Publicly Available Virtual Cohort of Four-chamber Heart Meshes for Cardiac Electro-mechanics Simulations, June 2020b. URL <https://zenodo.org/record/3890034>. Type: dataset.

- C. Bane Sullivan and Alexander Kaszynski. PyVista: 3d plotting and mesh analysis through a streamlined interface for the visualization toolkit (VTK). *Journal of Open Source Software*, 4(37):1450, May 2019.
- Edgar Tretschk, Ayush Tewari, Vladislav Golyanik, Michael Zollhöfer, Carsten Stoll, and Christian Theobalt. Patchnets: Patch-based generalizable deep implicit 3d shape representations. In *Computer Vision—ECCV 2020: 16th European Conference, Glasgow, UK, August 23–28, 2020, Proceedings, Part XVI 16*, pages 293–309. Springer, 2020.
- Benjamin Ummerhofer and Thomas Brox. Global, dense multiscale reconstruction for a billion points. In *Proceedings of the IEEE international conference on computer vision*, pages 1341–1349, 2015.
- Mathias Unberath, Andreas Maier, Dominik Fleischmann, Joachim Hornegger, and Rebecca Fahrig. Open-source 4d statistical shape model of the heart for x-ray projection imaging. In *2015 IEEE 12th International Symposium on Biomedical Imaging (ISBI)*, pages 739–742, 2015.
- Shuo Wang, Chen Qin, Nicolò Savioli, Chen Chen, Declan P. O’Regan, Stuart Cook, Yike Guo, Daniel Rueckert, and Wenjia Bai. Joint Motion Correction and Super Resolution for Cardiac Segmentation via Latent Optimisation. In Marleen de Bruijne, Philippe C. Cattin, Stéphane Cotin, Nicolas Padoy, Stefanie Speidel, Yefeng Zheng, and Caroline Essert, editors, *Medical Image Computing and Computer Assisted Intervention – MICCAI 2021*, pages 14–24, Cham, 2021. Springer International Publishing. ISBN 978-3-030-87199-4. doi: 10.1007/978-3-030-87199-4_2.
- Zhaohan Xiong, Martin K. Stiles, Yan Yao, Rui Shi, Aaqel Nalar, Josh Hawson, Geoffrey Lee, and Jichao Zhao. Automatic 3d surface reconstruction of the left atrium from clinically mapped point clouds using convolutional neural networks. *Frontiers in Physiology*, 13, 2022. ISSN 1664-042X.
- Xiahai Zhuang, Kawal S. Rhode, Reza S. Razavi, David J. Hawkes, and Sebastien Ourselin. A registration-based propagation framework for automatic whole heart segmentation of cardiac mri. *IEEE Transactions on Medical Imaging*, 29(9):1612–1625, 2010.
- Xiahai Zhuang, Jiahang Xu, Xinzhe Luo, Chen Chen, Cheng Ouyang, Daniel Rueckert, Victor M. Campello, Karim Lekadir, Sulaiman Vesal, Nishant RaviKumar, Yashu Liu, Gongning Luo, Jingkun Chen, Hongwei Li, Buntheng Ly, Maxime Sermesant, Holger Roth, Wentao Zhu, Jiexiang Wang, Xinghao Ding, Xinyue Wang, Sen Yang, and Lei Li. Cardiac segmentation on late gadolinium enhancement MRI: A benchmark study from multi-sequence cardiac MR segmentation challenge. *Medical Image Analysis*, 81:102528, October 2022. ISSN 1361-8415.

Appendix A. Dataset

Based on [Rodero et al. \(2021\)](#); [Strocchi et al. \(2020b\)](#), we built a public shape library of watertight 3D shapes for endo-/epicardium of the left/right ventricles (4 shapes in total). Note that the dataset is composed of 20 patients that are diagnosed as healthy (no cardiac conditions detected) [Rodero et al. \(2021\)](#) and 24 patients are diseased with various heart failures recruited for cardiac resynchronization therapy (CRT) upgrade [Strocchi et al. \(2020b,a\)](#). The generated shape data is available as a Zenodo record ([Grandits et al., 2024](#)).

A.1. Surface mesh generation

As a basis for our meshes, we used the publicly available data described in [Rodero et al. \(2021\)](#); [Strocchi et al. \(2020b\)](#). Our dataset was produced by applying the following procedure to each of the meshes: First, after loading the data, we localize the left ventricular apex using the available universal ventricular coordinates (UVCs, ([Bayer et al., 2018](#))) and use it as the Cartesian origin for each of the meshes. Next, we extract the left/right ventricular (LV/RV) endo-/epicardia by using the available surface tags. The provided meshes encode the walls and valves into separate tags, from which we extracted the surfaces. We then identify all points of the wall that touch the associated valve (e.g. LV wall with mitral and aortic valves). To identify all reachable points, we compute an eikonal solution using ([Grandits, 2021](#)) by placing an initial point on the inside of the wall (closest to the blood pool) with minimal velocity across points that touch any of the valves. The wall is then separated into epi- and endocardium by applying a thresholding filter on the solution. Finally, we remove non-manifold parts, recalculate the inside/outside orientation and close the surface to receive a watertight, proper manifold surface for the endo- and epicardia separately. Note that all steps exploit VTK ([Schroeder et al., 2006](#)) through PyVista ([Sullivan and Kaszynski, 2019](#)).

A.2. Surface sampling

The training data was then generated by sampling 3,000 surface points (surface samples) and additional 1,000 points, displaced in normal direction randomly (uniform) by up to 30mm (band samples) per surface, i.e. 16,000 points per patient. This point cloud was sampled with a curvature-based weighting to create more samples around features of interest (e.g. apex, valves). Specifically, we generated the dataset samples using face-weights w following [Gao et al. \(2019, Eq. 2.6\)](#) that are defined as follows: consider a 2-dimensional compact surface M , isometrically embedded in \mathbb{R}^3 , with its Gaussian curvature κ and mean curvature η . The weighting function is then defined as

$$w_{\lambda,\rho}(\mathbf{x}) = \frac{\lambda|\kappa(\mathbf{x})|^\rho}{\int_M |\kappa(\xi)|^\rho \mathrm{dvol}_M(\xi)} + \frac{(1-\lambda)|\eta(\mathbf{x})|^\rho}{\int_M |\eta(\xi)|^\rho \mathrm{dvol}_M(\xi)}. \quad (4)$$

In our experiments, we used $w_{0.1,0.75}$ as the curvature weight, purely by visual inspection. We used the library `trimesh` ([Dawson-Haggerty et al., 2009](#)) for sampling and computing κ and η .

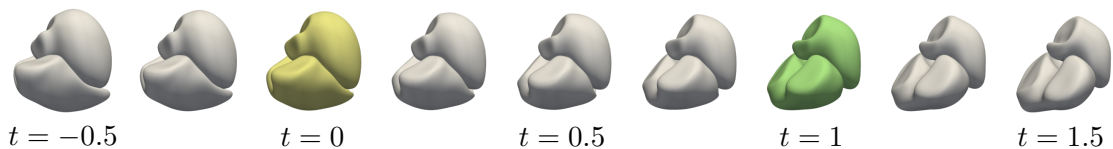


Figure 4: The figure shows the generation of heart models via interpolation and extrapolation of latent code vectors. In detail, we take two latent code representations $\mathbf{z}_1, \mathbf{z}_2$ from the training dataset and decode the linear combinations $t\mathbf{z}_1 + (1-t)\mathbf{z}_2$. We present the reconstructed endocardia.

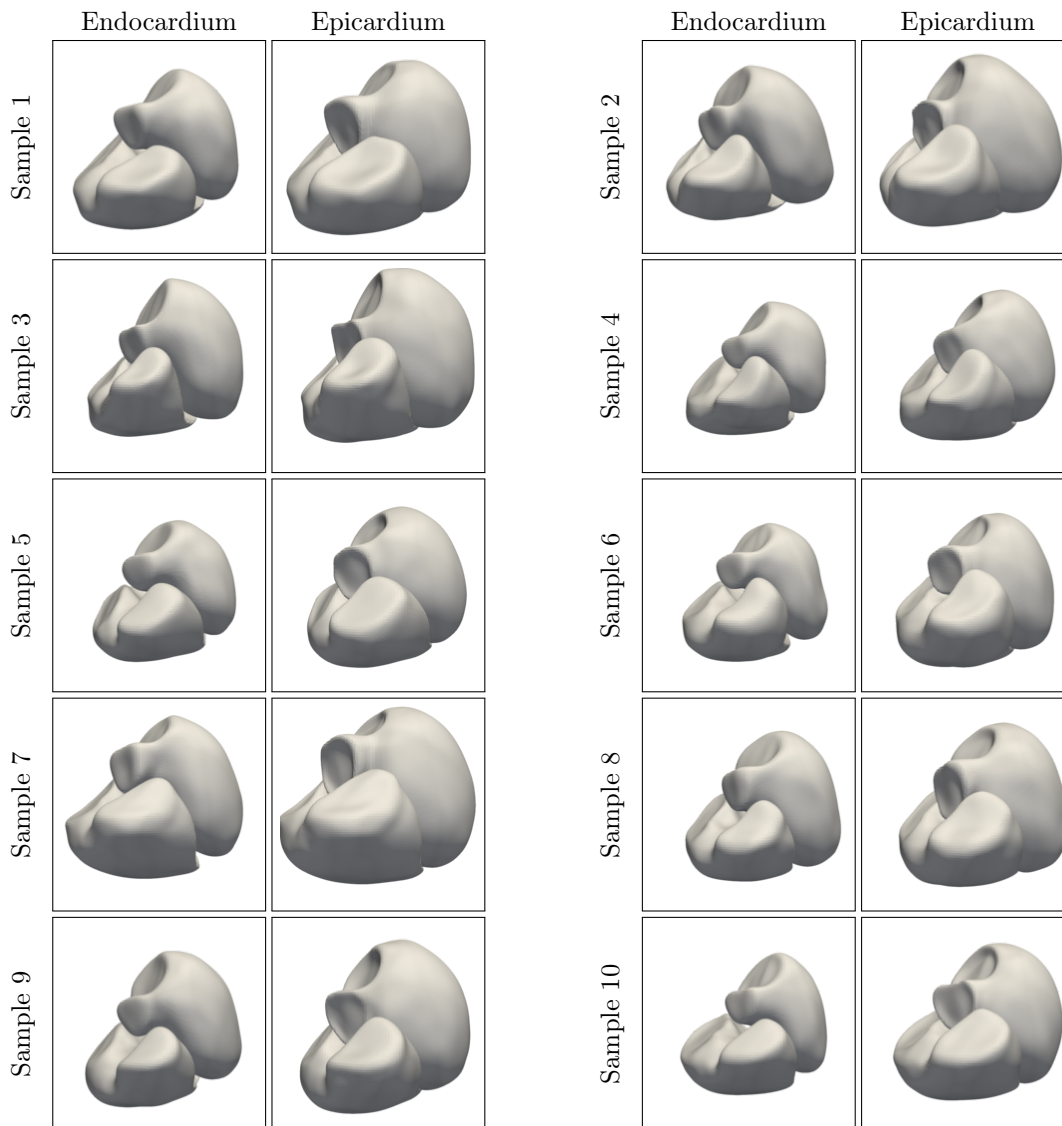


Figure 5: We reconstruct points in the latent space that are sampled from a zero-mean Gaussian distribution with covariance $\sigma^2 I$.

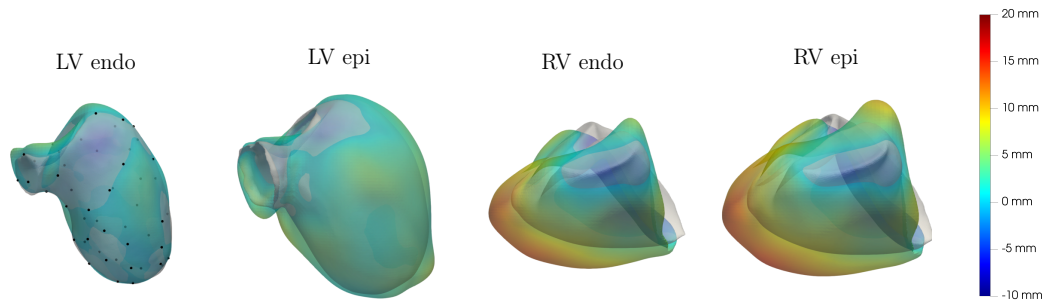


Figure 6: We reconstruct all four surfaces from 50 points on the endocardium of the left ventricle. The reconstructed meshes are color-coded with the mesh distance, i.e. the distance to the nearest point on the ground truth mesh in mm.

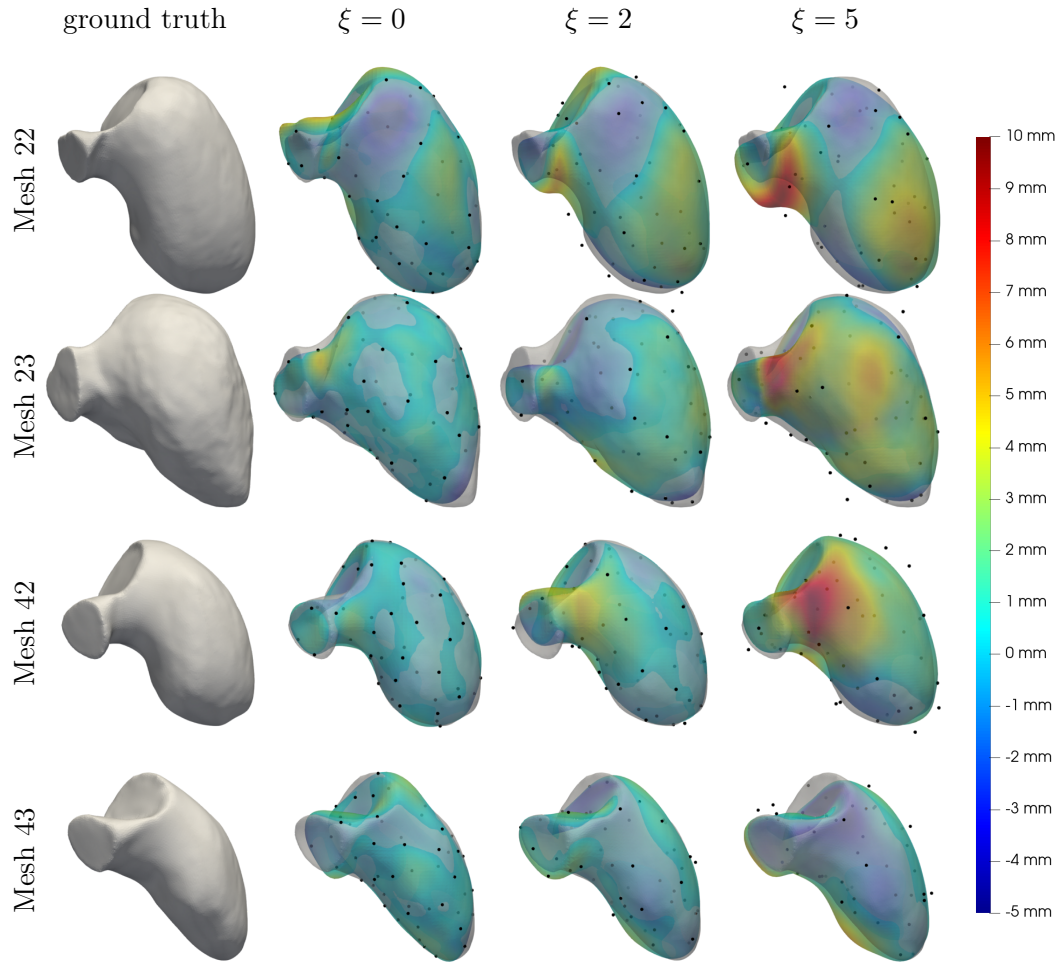


Figure 7: Reconstruction quality of the left ventricle from 50 points with different levels of noise. We color-coded the implicit distance to the ground truth mesh.

Appendix B. Metrics

To quantify the quality of reconstructed meshes we use the *L2-Chamfer-distance* (CD), the *Hausdorff-distance* (HD), and a *Large deformation diffeomorphic metric mapping* (LDDMM) loss terms between the reconstructed mesh and the ground truth mesh. We calculate the L2-Chamfer distance and the Hausdorff distance by sampling 50 000 points on each mesh. For two point clouds \mathbf{X} and \mathbf{Y} the CD is given as

$$d_{\text{CD}}(\mathbf{X}, \mathbf{Y}) = \frac{1}{|\mathbf{X}|} \sum_{x \in \mathbf{X}} \min_{y \in \mathbf{Y}} \|x - y\|_2 + \frac{1}{|\mathbf{Y}|} \sum_{y \in \mathbf{Y}} \min_{x \in \mathbf{X}} \|x - y\|_2.$$

The Hausdorff distance (HD) is defined as

$$d_{\text{HD}}(\mathbf{X}, \mathbf{Y}) = \max\{\max_{x \in \mathbf{X}} \min_{y \in \mathbf{Y}} \|x - y\|_2, \max_{y \in \mathbf{Y}} \min_{x \in \mathbf{X}} \|x - y\|_2\}.$$

With the LDDMM loss, we measure how well the reconstructed mesh \mathcal{M}_r can be registered to the original ground truth mesh \mathcal{M}_{gt} . To obtain numerically comparable results across the different methods we first remesh the results to obtain meshes with the same resolution (for this task, we use the Blender software package ([Blender Online Community, 2018](#)) with a voxel resolution of 0.9 mm). To obtain the LDDMM loss, we calculate the center points c_F , the normals n_F and the area A_F of every face F from the set of faces \mathcal{F}_r and \mathcal{F}_{gt} , respectively. For $\gamma = 1$ let

$$C(\mathcal{F}_1, \mathcal{F}_2) = \sum_{F_1 \in \mathcal{F}_1} \sum_{F_2 \in \mathcal{F}_2} e^{-\gamma \|c_{F_1} - c_{F_2}\|_2^2} \langle n_{F_1}, n_{F_2} \rangle A_{F_1} A_{F_2}.$$

Then, the LDDMM loss is defined as

$$d_L(\mathcal{M}_{gt}, \mathcal{M}_r) = C(\mathcal{F}_{gt}, \mathcal{F}_{gt}) + C(\mathcal{F}_r, \mathcal{F}_r) - 2C(\mathcal{F}_{gt}, \mathcal{F}_r).$$

Appendix C. Fitting the Statistical Shape Model

The statistical shape model describes a heart shape as a variation of a mean shape μ in different directions (modes). We used the publicly available SSM from the cardiac atlas project that is based on 630 healthy Biobank reference patients, further described in [Petersen et al. \(2017\)](#). A mean point cloud $\mathbf{X} \in \mathbb{R}^{N \times 3}$ of N points together with 200 eigenmodes $\mathbf{V}_i \in \mathbb{R}^{N \times 3}$ for $i = 1, \dots, 200$ and corresponding eigenvalues $\lambda \in \mathbb{R}^{200}$ are provided, which is restricted to the subset of points corresponding to the endocardium of the left ventricle. For a given sample with weights $\alpha \in \mathbb{R}^{200}$ and a spatial offset $\mathbf{b} \in \mathbb{R}^3$, we obtain a representation of the resulting point cloud \mathbf{C} as $\mathbf{C} = \mathbf{X} + \mathbf{1}_N \mathbf{b}^\top + \sum_{i=1}^{200} \alpha_i \lambda_i \mathbf{V}_i$. For a given target point cloud \mathbf{Y} we use this model to optimize the asymmetric Chamfer distance $d_{\text{aCD}}(\mathbf{Y}, \mathbf{C}) = \frac{1}{|\mathbf{Y}|} \sum_{y \in \mathbf{Y}} \min_{x \in \mathbf{C}} \|x - y\|_2$ w.r.t. the weights α and the spatial offset \mathbf{b} . Additionally, we use a standard ℓ_2 loss term to obtain the final objective function

$$\mathcal{J}_{\mathbf{Y}}(\alpha, \mathbf{b}) = d_{\text{aCD}} \left(\mathbf{Y}, \mathbf{X} + \mathbf{1}_N \mathbf{b}^\top + \sum_{i=1}^{200} \alpha_i \lambda_i \mathbf{V}_i \right) + \beta \|\alpha\|_2.$$

This loss function is optimized for 5 000 epochs with the Adam optimizer ([Kingma and Ba, 2015](#)), with a learning rate of 0.005.

	ξ	n	Points2Surf	Point2Mesh	SSM	ours*	ours
Chamfer Distance	0	50	-	1.74±0.41	3.58±1.04	<i>1.20</i> ±0.91	0.75 ±0.18
		200	-	<i>0.68</i> ±0.11	2.73±0.77	0.72±0.54	0.49 ±0.09
		500	1.66±0.32	<i>0.57</i> ±0.08	2.34±0.76	0.70±0.57	0.45 ±0.09
		2000	0.79±0.17	0.57±0.11	1.87±0.83	<i>0.54</i> ±0.32	0.43 ±0.07
	2	50	-	2.33±0.54	3.60±1.38	<i>1.65</i> ±0.87	1.38 ±0.28
		200	-	<i>1.16</i> ±0.13	2.79±0.82	<i>1.16</i> ±0.57	0.96 ±0.17
		500	1.65±0.14	<i>0.97</i> ±0.10	2.33±0.68	<i>0.97</i> ±0.33	0.96 ±0.11
		2000	1.85±0.42	0.80 ±0.13	1.88±0.86	<i>1.11</i> ±0.78	1.48±0.52
	5	50	-	3.50±0.49	3.79±1.34	<i>2.60</i> ±0.98	2.39 ±0.48
		200	-	3.17±0.62	3.00±0.88	<i>1.87</i> ±0.39	1.84 ±0.27
		500	2.82±0.31	3.85±1.15	2.49±0.70	<i>2.32</i> ±1.00	1.99 ±0.33
		2000	3.22±0.32	5.07±0.94	2.08 ±0.92	4.24±1.50	<i>3.10</i> ±0.79
Hausdorff Distance	0	50	-	10.86±3.45	11.96±3.69	<i>7.54</i> ±7.25	4.40 ±1.82
		200	-	<i>4.23</i> ±1.18	9.93±3.88	4.52±5.79	2.57 ±0.92
		500	9.88±3.84	2.45 ±0.55	9.81±5.45	<i>4.14</i> ±5.01	4.43±15.03
		2000	6.30±0.73	1.66 ±1.11	11.29±9.16	2.99±2.91	<i>2.00</i> ±0.79
	2	50	-	12.86±3.99	12.27±4.58	<i>7.75</i> ±4.40	6.01 ±2.54
		200	-	<i>5.82</i> ±1.17	10.27±4.04	6.07±4.20	4.36 ±1.32
		500	10.29±1.02	<i>4.53</i> ±1.12	9.69±5.07	5.31±5.27	4.41 ±1.14
		2000	10.04±0.73	5.15 ±2.06	11.52±9.21	<i>7.03</i> ±5.38	10.82±5.50
	5	50	-	16.13±3.09	12.61±4.10	<i>10.58</i> ±5.41	8.72 ±2.22
		200	-	14.94±2.85	11.25±4.35	<i>8.34</i> ±2.56	7.78 ±1.91
		500	18.68±2.10	15.83±2.56	10.78±5.02	<i>10.43</i> ±4.96	8.66 ±2.12
		2000	19.77±1.46	17.95±3.34	13.20 ±9.14	19.64±6.48	<i>15.29</i> ±4.12
LDDMM Loss ($\times 10^3$)	0	50	-	73.5±24.97	99.21±31.57	<i>53.39</i> ±25.22	35.01 ±14.96
		200	-	34.82±14.33	93.53±30.00	<i>29.81</i> ±20.54	17.20 ±8.81
		500	75.51±25.72	<i>26.01</i> ±11.80	89.67±29.86	27.16±25.30	12.42 ±6.49
		2000	<i>14.07</i> ±7.05	25.16±12.85	80.41±26.87	18.93±15.98	11.84 ±7.21
	2	50	-	88.64±26.12	99.05±31.77	<i>72.63</i> ±24.63	68.98 ±22.57
		200	-	65.05±19.99	94.76±30.62	<i>57.96</i> ±21.68	51.56 ±17.79
		500	78.18±23.83	55.72±18.50	90.19±30.38	50.98 ±16.10	<i>52.68</i> ±14.37
		2000	38.39 ±12.96	<i>43.59</i> ±15.17	80.19±26.93	51.79±19.65	63.63±13.81
	5	50	-	109.14±27.98	101.57±37.27	<i>91.93</i> ±26.39	90.50 ±24.21
		200	-	108.31±26.01	97.98±34.19	<i>82.23</i> ±21.85	82.23 ±21.26
		500	89.19±25.25	114.69±18.64	92.37±32.41	<i>88.77</i> ±19.81	84.5 ±21.61
		2000	76.54 ±18.93	131.00±27.89	<i>83.01</i> ±26.17	122.25±37.38	98.92±20.20

Table 1: Mean and standard deviation of the Chamfer distance (CD), the Hausdorff distance, and the LDDMM-loss for different numbers of input points n and different levels of noise ξ . For every test case, the lowest value is printed in bold and the second lowest value is printed in italic. The asterisk denotes the non Lipschitz regularized version of our network.

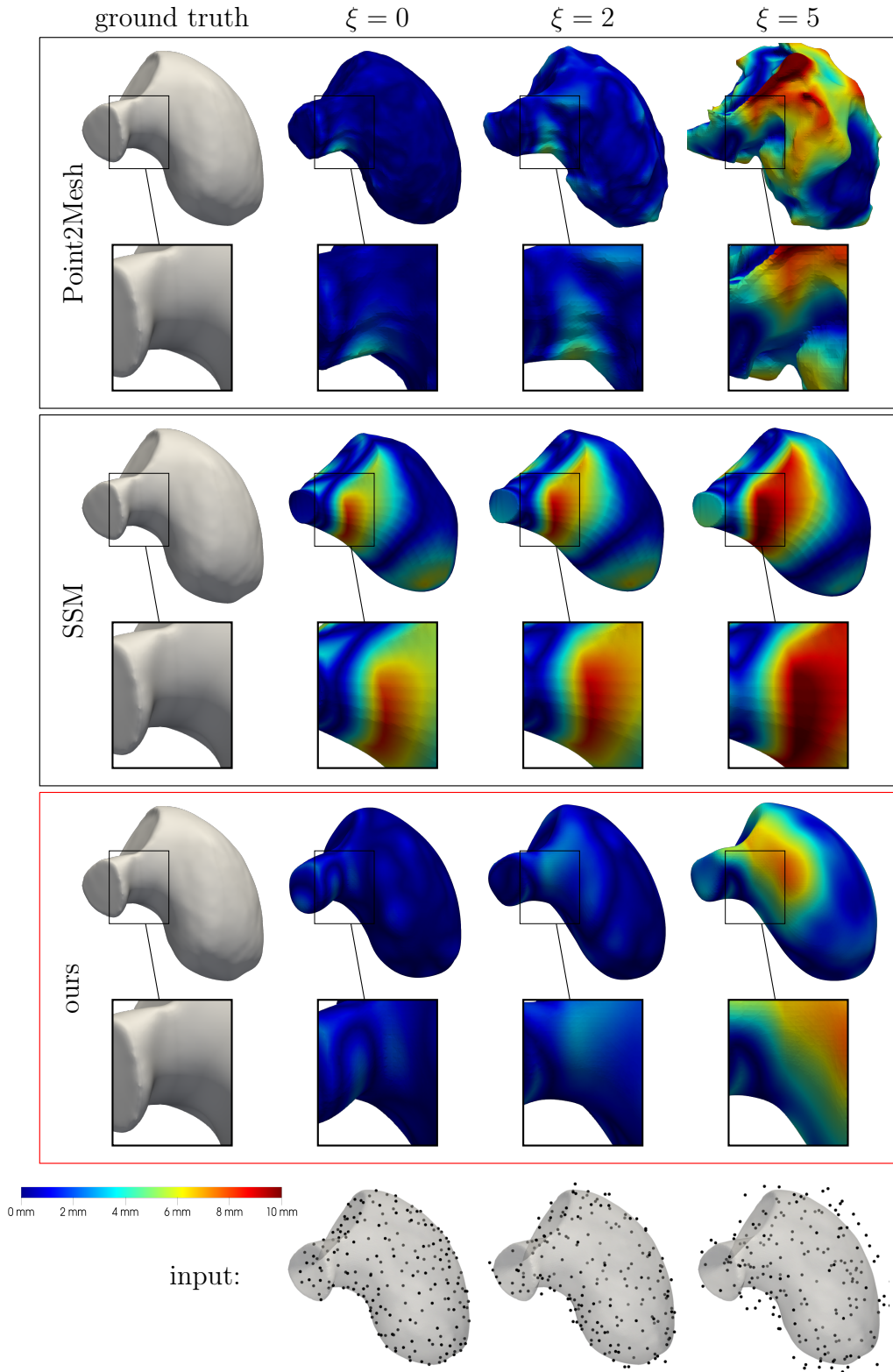


Figure 8: Mesh quality for different methods on mesh 43. We depict the result for 200 points. We color-coded the absolute distance to the ground truth mesh on the remeshed results.

Appendix D. Multichamber Experiments

In this section, we investigate the advantages of jointly encoding of left and right endocardial shapes in comparison to independently reconstructing the two shapes. We then compare the average chamfer distances across both endocardia for the case of a separate reconstruction and a joint reconstruction for four test meshes. Additionally, we perform the same experiment on partially observable regions, where the points on the left ventricle are only sampled from its top half (ventricular base) and the points of the right ventricle are sampled from its lower half (ventricular apex). The results of both experiments can be found in Table 2. For the case of full data availability, the joint reconstruction seems to be advantageous only for the case of very sparse data ($n = 10$), but for the cases where only partial data is available, the joint reconstruction improves the resulting reconstruction in all but two cases.

		full data		partial data	
σ	n	CD_{separate}	CD_{joint}	CD_{separate}	CD_{joint}
0	10	2.71	2.47	3.31	2.50
	20	1.57	1.86	2.76	2.38
	30	1.43	1.42	2.34	2.77
	40	1.17	1.31	2.41	2.46
2	10	3.13	3.06	4.16	2.81
	20	2.43	2.39	3.24	2.72
	30	2.01	2.01	3.35	2.50
	40	1.83	2.12	3.24	2.82
5	10	3.63	3.49	3.95	3.92
	20	3.42	3.47	4.51	4.12
	30	3.04	3.25	3.76	3.70
	40	2.86	2.87	3.89	3.71

Table 2: Average reconstruction quality per surface for inference based on n points on the LV Endocardium only.

Appendix E. Obtaining the EAM data

The EAM data has been acquired with the NOGA-XP system (Biologic Delivery Systems, Biosense Webster) equipped with a conventional 7-Fr deflectable-tip mapping catheter (NAVI-STAR, Biosense Webster). Spatial positions of the tip of the catheter were acquired at 100 Hz, and aligned in time using the automatically detected R-peak of the 12-lead ECG. Points were accepted by the system according to a set of criteria for catheter stability and signal quality. The institutional review board approved the study protocol, and all patients gave written and oral informed consent for the investigation (the study is compliant with the Declaration of Helsinki). Further information on the study has been previously reported [Maffessanti et al. \(2020\)](#); [Pezzuto et al. \(2021\)](#). We pre-processed the data by applying a -90° rotation about the X -axis (NOGA to LPS-MRI coordinate system), fol-

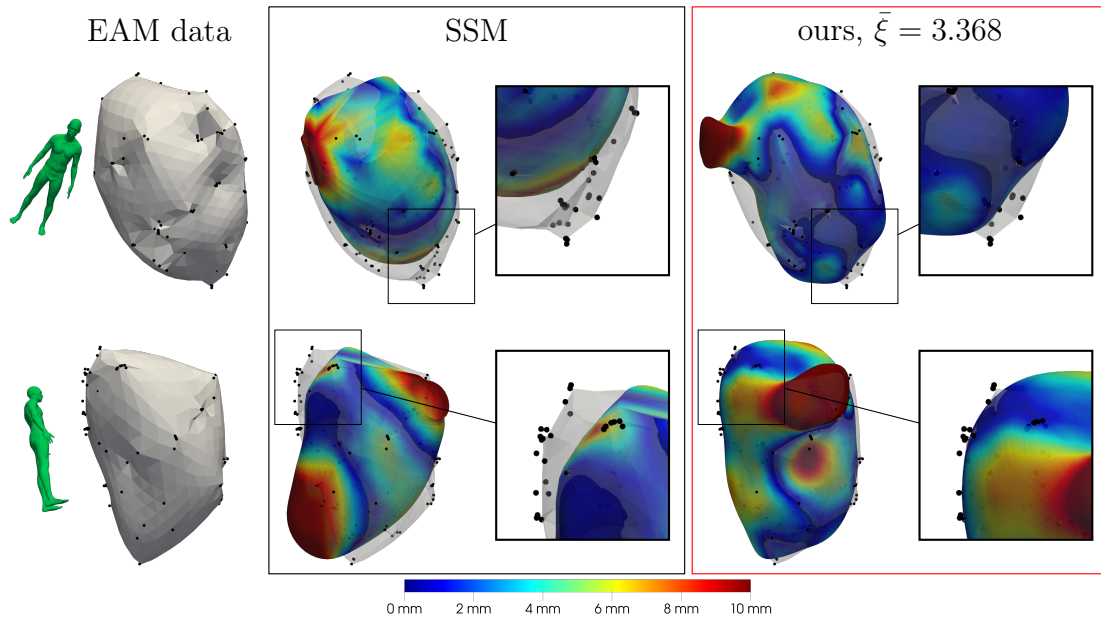


Figure 9: Reconstruction of the LV endocardium from the EAM data. We compare the SSM reconstruction (left panel) to our approach for an optimal noise level estimation of $\bar{\sigma} = 3.368$ mm (right panel). We also report the absolute distance from the geometry provided by the EAM system.

lowed by a translation to align the LV epicardial apex with the origin. Note that only an approximate alignment is possible since the epicardium is not present in the EAM data.

Appendix F. Estimation of noise level

In Table Table 3 we present the numerical convergence of the noise estimator $\bar{\xi}_i$ for the first six steps on the EAM data (c.f. Section 4.3). Additionally, the performance of this method is tested for a synthetic point cloud (Heart 43, $n = 500$, $\xi = 5$), where the correct noise level is obtained.

step	synthetic		EAM data	
$\bar{\xi}_0$	0	15	0	15
$\bar{\xi}_1$	3.159	4.882	1.499	4.672
$\bar{\xi}_2$	4.878	5.063	3.184	3.686
$\bar{\xi}_3$	5.063	5.060	3.344	3.398
$\bar{\xi}_4$	5.060	5.060	3.797	3.367
$\bar{\xi}_5$	5.060	5.060	3.410	3.364
$\bar{\xi}_6$	5.060	5.060	3.368	3.364

Table 3: Iteration of the variance estimation for the synthetic case (Heart 43, $n = 500$, $\xi = 5$) and the EAM data.